

Microwave breast cancer detection using Empirical Mode Decomposition features

Hongchao Song¹ · Yunpeng Li² · Mark Coates² · Aidong Men¹

Received: date / Accepted: date

Abstract Microwave-based breast cancer detection has been proposed as a complementary approach to compensate for some drawbacks of existing breast cancer detection techniques. Among the existing microwave breast cancer detection methods, machine learning-type algorithms have recently become more popular. These focus on detecting the existence of breast tumours rather than performing imaging to identify the exact tumour position. A key step of the machine learning approaches is feature extraction. One of the most widely used feature extraction method is principle component analysis (PCA). However, it can be sensitive to signal misalignment. This paper presents an empirical mode decomposition (EMD)-based feature extraction method, which is more robust to the misalignment. Experimental results involving clinical data sets combined with numerically simulated tumour responses show that combined features from EMD and PCA improve the detection performance with an ensemble selection-based classifier.

Keywords Microwave breast cancer detection · Empirical mode decomposition · Principle component analysis · Support vector machine

1 Introduction

Detecting breast cancer during the early stages of development is one of the best ways to improve the recovery rate [27]. Among the widely used breast cancer screening

methods, magnetic resonance imaging (MRI) is very expensive, and X-ray mammography involves exposure to radiation and painful breast compression. Neither can be frequently used as a routine detection method. Ultrasound is inexpensive but is less accurate and can struggle to differentiate between benign and malignant lesions [21]. Microwave-based breast cancer detection methods have been intensively explored over the past two decades as a potential complementary screening modality. The basis of this method is the reported significant differences in dielectric properties between malignant and healthy breast tissue in the microwave frequency range [13,32].

In the existing research in the field of microwave breast cancer screening, two different directions have been explored: imaging methods [3, 4, 6, 15, 18, 21–23, 30] and machine learning methods [1, 5, 8, 9, 11, 20]. In both cases, transmitting antennas illuminate the breast area using ultra-wideband microwave signals and receiving antennas record the reflected signals. In the imaging methods, algorithms are applied to construct an image of the breast that can be used to determine the existence and position of a tumour. The imaging algorithms fall into two categories: tomography and radar (backscatter). The tomography methods try to estimate the electromagnetic parameters of the entire breast using inverse scattering algorithms. This is an ill-posed problem, and leads to challenges in robust inference and a high computational cost [6, 22, 30]. Radar imaging methods [3, 4, 15, 18, 21, 23] use confocal algorithms to determine the position of the significant scatterers in the breast. These indicate regions of high contrast in dielectric properties that may be caused by the presence of malignant tissue. Alternative imaging algorithms, based respectively on Bayesian modeling and time reversal techniques, have been proposed in [10, 16].

Another direction is the application of machine learning techniques. Here the goal is usually detection of the presence of a tumour, as opposed to identifying its location. A

✉Hongchao Song · Aidong Men

¹School of Information and Communication Engineering, Beijing University of Posts and Telecommunications, Beijing, China
E-mail: shch@bupt.edu.cn, menad@bupt.edu.cn

Yunpeng Li · Mark Coates

²Dept. of Electrical and Computer Engineering, McGill University, Montréal, Québec, Canada
E-mail: yunpeng.li@mail.mcgill.ca, mark.coates@mcgill.ca

key component of machine learning algorithms is feature extraction. This process generates useful features in a lower dimension than that of the original data. In a wide variety of applications, the quality of the extracted features has been shown to have a dramatic effect on the performance of classifiers. Thus, the feature extraction method adopted should be robust to the data characteristics in the target application.

Local discriminant bases (LDB) were used to identify features in [11]; these strive to find orthonormal principal components of the data with localized time-frequency characteristics. The discrete cosine transform (DCT) was applied to extract features in [1]. The most widely used feature extraction method in microwave breast cancer detection is principal component analysis (PCA) [5, 8, 9, 11, 20]. PCA reduces the data dimension by projecting the data onto a subspace that retains the maximum variance of the signal collection. The PCA methods have provided the most promising results, but a significant deficiency is the sensitivity to misalignment between signals. Misalignment is common in microwave breast scans due to mechanical issues such as antenna movement between scans and the system intrinsic jitter in the clock and the sampling oscilloscope [26, 28]. Thus, there can be a great disparity between the features extracted from two scans of the same healthy breast, arising simply because the recordings are slightly shifted in time. In most of the previously reported results [5, 8, 9, 11], this has not been a significant issue because the analysis used numerically simulated data or phantom measurements.

Inspired by the successful application of empirical mode decomposition (EMD) in Electroencephalography (EEG) signal processing [2, 17], we explore the incorporation of EMD into our feature extraction method for microwave breast cancer detection. The EMD method is a data-driven technique that decomposes the non-stationary signal into a usually small number of intrinsic mode functions (IMFs) [14]. The EMD method is insensitive to misalignment of signals, as it is applied to each signal independently. If we shift a signal by a few time samples, the IMFs obtained from the shifted signal will be time-shifted copies of those obtained from the original signal. If we specify features as statistical properties of the IMFs that are insensitive to the time-shift, such as mean absolute values and standard deviations, then the feature extraction procedure is robust to the presence of jitter in the measurement process. In contrast, PCA processes multiple signals jointly; changing any signal results in different PCA components and scores for all measurements.

Given these desired characteristics of EMD, we propose combining EMD-based features with PCA-based features for microwave breast tumour detection, to exploit the complementary strengths of both feature extraction approaches. EMD-based feature extraction focuses on the characteristics of a single measurement. PCA-based feature extraction focuses on the variances among different samples. We test the

performance of the proposed method and discuss the results obtained in our experiments.

2 Methods

2.1 Feature extraction and classification

2.1.1 Empirical mode decomposition

The empirical mode decomposition is an iterative procedure, as described in Algorithm 1 [14]. During each iteration a decomposition signal is constructed. This decomposition signal is identified as an IMF if it satisfies two conditions:

- C1: The difference between the number of extrema (maxima and minima) and the number of zero-crossings must be no more than one;
- C2: The local mean, defined as the mean of the upper and lower envelopes, must be zero.

Algorithm 1 Empirical mode decomposition

Input: Signal x .

Input: Maximum number of IMFs: N_{IMF} .

- 1: Set $k = 0$ and $r_0 = x$. Set $z = x$.
 - 2: **while** $k < N_{\text{IMF}}$ **do**
 - 3: Find all extrema of z .
 - 4: Interpolate between minima (maxima) of z to obtain the lower (upper) envelope e_{\min} (e_{\max}).
 - 5: Compute the mean envelope $m = (e_{\min} + e_{\max})/2$.
 - 6: Compute the IMF candidate $d_{k+1} = z - m$.
 - 7: Is d_{k+1} an IMF? (does it satisfy C1 and C2?)
 - Yes. Save d_{k+1} ; compute the residue $r_{k+1} = x - \sum_{i=1}^k d_i$. Set $z = r_{k+1}$.
 - No. Set $z = d_{k+1}$.
 - 8: **end while**
-

An example of the EMD decomposition of an antenna-pair recording is shown in Figure 1. The IMFs can be viewed as a set of components of the signal, each capturing different time-scale characteristics and local structure. [14].

2.1.2 Feature extraction

Following the practice in [17], we calculate the first 5 IMFs of the EMD for each measurement. For each IMF, 4 features are calculated. They are the mean absolute value (μ), the standard deviation (σ), the kurtosis (κ) and the mean absolute successive difference (S). The mean absolute successive difference is used to measure the intensity of signal changes. The features for the k -th IMF, of length L time samples, are:

1. Mean absolute value (μ_k):

$$\mu_k = \frac{1}{L} \sum_{i=1}^L |d_k(i)|, \quad (1)$$

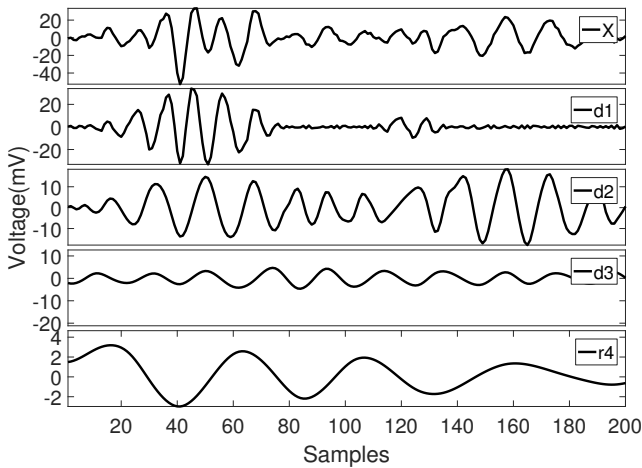


Fig. 1: Example of EMD. X is a healthy measurement collected by the antenna pair A16A15 from the left breast of volunteer two during her first visit; $d1 - d3$ are the first three IMFs (modes); and $r4$ is the residue.

2. Standard deviation (σ_k):

$$\sigma_k = \sqrt{\frac{1}{L} \sum_{i=1}^L (d_k(i) - \frac{1}{L} \sum_{i=1}^L d_k(i))^2}, \quad (2)$$

3. Kurtosis (κ_k):

$$M_k = \frac{1}{L} \sum_{i=1}^L d_k(i) \quad (3)$$

$$\kappa_k = \frac{\frac{1}{L} \sum_{i=1}^L (d_k(i) - M_k)^4}{(\frac{1}{L} \sum_{i=1}^L (d_k(i) - M_k)^2)^2}$$

4. Mean absolute successive difference (S_k):

$$S_k = \frac{1}{L-1} \sum_{i=1}^{L-1} |d_k(i+1) - d_k(i)|. \quad (4)$$

The magnitudes of the features derived from IMFs obtained later in the decomposition procedure are most often smaller in magnitude. For the measurements which are collected by the same antenna pair, we rescale each feature of the training data into the range $[0, 1]$. The testing data is scaled by the same ratio. The process is repeated for each antenna pair.

We also perform PCA on the signals derived from each antenna pair. 30 principal scores are retained, as in [19]. The PCA scores are also normalized, by scaling the first principal components to the range $[0, 1]$. The PCA scores of the other dimensions are rescaled by the same ratio. For PCA features, a coefficient matrix is calculated from the training data. This is formed from the measurements collected by the same antenna pair from all volunteers, and both

healthy measurements and tumour response-injected measurements are included. The PCA features associated with a single antenna pair measurement are thus dependent on all of the other measurements for that antenna pair. In contrast, the EMD features corresponding to a single time-series recorded by an antenna pair are independent of any other measurements. When we consider combining the features, each antenna pair time series measurement is represented by a 50 dimensional feature vector, combining the 30 PCA features and the 20 EMD features.

2.1.3 Classification

The classifier we adopt is the cost-sensitive ensemble selection-based classifier proposed in [19]. This demonstrates better classification performance than imaging-based classifiers and other ensemble classification structures. The ensemble selection-based classifier constructs base classifiers by choosing different antenna pairs and different hyper parameters in a cost-sensitive 2ν - support vector machine (SVM) [7]. The hyper-parameters ν_+ and ν_- control the importance associated with the two types of classification error (false-positive and false-negative) while the hyper-parameter γ is the kernel width of the SVM. The model selection stage chooses the base models with the smallest Neyman-Pearson measure \hat{e} [29]

$$\hat{e} = \frac{1}{\alpha} \max\{\hat{P}_F - \alpha, 0\} + \hat{P}_M, \quad (5)$$

where \hat{P}_M is the empirical miss probability, \hat{P}_F is the empirical false positive rate, and α is the upper bound of the target false positive rate. The classification algorithm is depicted in Figure 2.

2.2 Experimental data

The experimental data were collected with a multi-static radar system with $R = 16$ antennas [25] built by the research team at McGill University. For one scan, each of the R antennas transmits an ultra-wideband pulse into the breast, and the other antennas record the backscattered signals. This process is repeated until one measurement is recorded by each of the $M = R(R - 1) = 240$ different antenna pairs.

We performed breast scans on 12 healthy volunteers. Table 1 lists the number of visits for each volunteer. The clinical trial lasted 8 months, and involved 48 patient visits, with each volunteer visiting at most once per month [24]. We collected measurements of the left breast and the right breast from the same person during each visit. Thus, $48 \times 2 = 96$ sets of measurements were collected.

Since all participants of the clinical trial were healthy volunteers, there are only tumour-free measurements in our original data set. We adopt the strategy outlined in [19] to

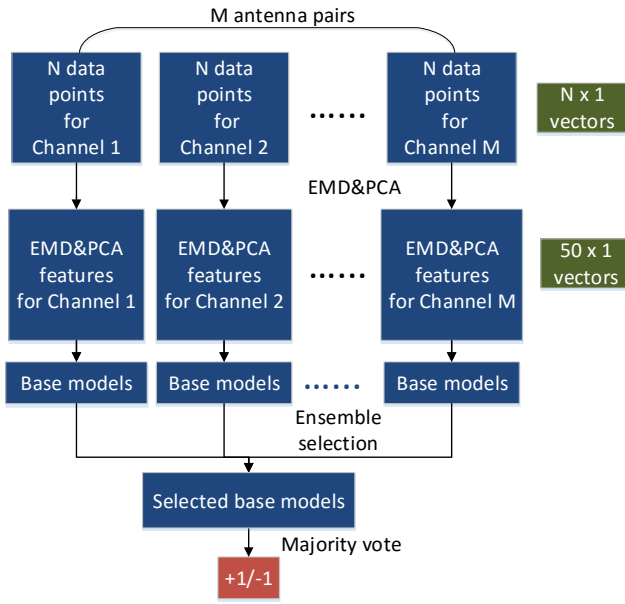


Fig. 2: The combined feature extraction and classification procedure.

Table 1: Number of visits for each volunteer

Volunteer index	1	2	3	4	5	6
Number of visits	3	3	4	5	2	6
Volunteer index	7	8	9	10	11	12
Number of visits	6	4	4	4	3	4

simulate tumour responses for each volunteer, based on the transmitted pulses from the antennas and the dielectric properties of breast tissue. For one antenna pair and a tumour position p_0 , the frequency domain representation of the tumour response $R^t(p_0, \omega)$ is modeled as:

$$R^t(p_0, \omega) = \Gamma R(\omega) e^{-j(k_{im}(d_{im}^t - d_{im}^d) + k_{br}(d_{br}^t - d_{br}^d))}, \quad (6)$$

where $R(\omega)$ is the frequency domain representation of received signal, d_{im}^d and d_{br}^d are the lengths of the direct path for this antenna pair through the immersion medium (ultrasound gel) and breast tissue, respectively. d_{im}^t and d_{br}^t are the lengths of the shortest path between the antenna pair via the tumour position p_0 , in the immersion medium and the breast tissue, respectively. Γ is a constant that can be used to introduce additional attenuation in the tumour response. In this paper, we concentrate on the case $\Gamma = 1$. k_{im} and k_{br} are the wavenumbers for the immersion medium and breast tissue, respectively, and these have the following expressions:

$$k_{im}(\omega) = \frac{2\pi}{\lambda_{im}(\omega)} = \sqrt{\epsilon_{im}(\omega)} \frac{\omega}{c}, \quad (7)$$

$$k_{br}(\omega) = \frac{2\pi}{\lambda_{br}(\omega)} = \sqrt{\epsilon_{br}(\omega)} \frac{\omega}{c}. \quad (8)$$

Here ϵ_{im} is the relative permittivity of the immersion medium, c is the speed of light, and ϵ_{br} is the average breast tissue relative permittivity. The latter is specified by the Debye model [12]:

$$\epsilon_{br}(\omega) = \epsilon_{\infty} + \frac{\Delta\epsilon}{1 + j\omega\tau} + \frac{\sigma_s}{j\omega\epsilon_0}, \quad (9)$$

where $\epsilon_0 = 8.854 \times 10^{-12}$ F/m is the permittivity of free space, and ϵ_{∞} is the dielectric constant of the material at infinite frequency. $\Delta\epsilon = \epsilon_s - \epsilon_{\infty}$, and ϵ_s is the static dielectric constant. The pole relaxation constant is τ and the static conductivity is σ_s . The model parameters are chosen to approximate the dielectric properties of breast tissue.

We refer readers to [19] for a more complete description and discussion of the tumour response simulation procedure. We do stress that this is not a model that assumes homogeneous breast tissue. By including the *received* signal $R(\omega)$, rather than the transmitted signal, the model incorporates distortions and delays caused by inhomogeneous tissue. In Figure 3, we present one example of a tumour response injected signal.

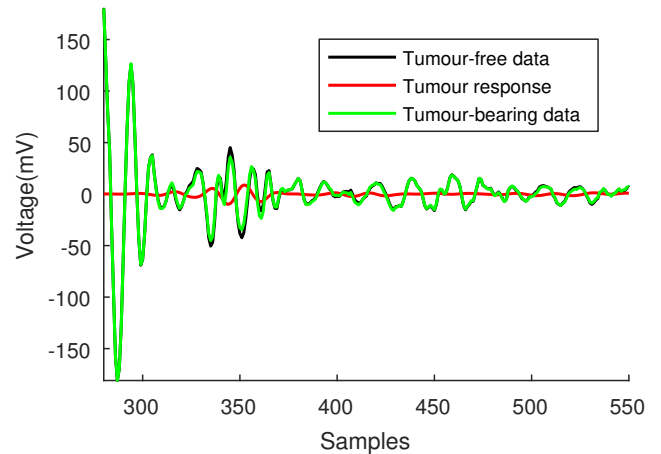


Fig. 3: An example of received pulses before and after tumour response injection. The pulse is collected by the antenna pair A1A2 from the left breast of volunteer one during her first visit.

In order to evaluate the classification performance with different feature extraction methods, we generate 50 datasets with different breast relative permittivity values and different tumour positions for the same volunteer. For each data set, half of each volunteer's visits are randomly selected as tumour-bearing visits. If the number of visits N_j for patient j is an odd number, $\frac{N_j-1}{2}$ visits are selected as tumour-bearing visits. In these tumour-bearing visits, we randomly select one breast as the tumour-bearing breast, and randomly sample a tumour position in the upper-quadrant region of the

breast, closer to the armpit, which is reported to be the most likely breast tumour region [31]. The Debye model parameters are randomly generated for different volunteers. The ranges of possible parameter values are detailed in [19]. The breast permittivities are different for different volunteers.

In evaluating the classification performance, we divide each data set into $\binom{12}{2} = 66$ training-testing pairs, by using data from 10 volunteers to form the training data, and data from 2 volunteers to form the testing data. To construct testing data, we further add tumour-bearing scans for each tumour-free scan, so that the ratio of tumour-free scans and tumour-bearing scans is 1:1 in the test data. This allows us to more extensively test classification performance. To achieve this, we randomly generate tumour positions for each scan so that different tumour positions may exist for the same volunteers. However, we keep the same relative permittivity for the same volunteer in the training and testing set. We do not add more tumour-bearing data in the training data, so that the ratio of tumour-free scans and tumour-bearing scans in the training data is 3:1. This forms an imbalanced training data set to train the classifier and mimics the real scenario where the number of tumour-free scans is more than the number of tumour-bearing scans. A graphical illustration for one training-testing pair of one data set is provided in Figure 4.

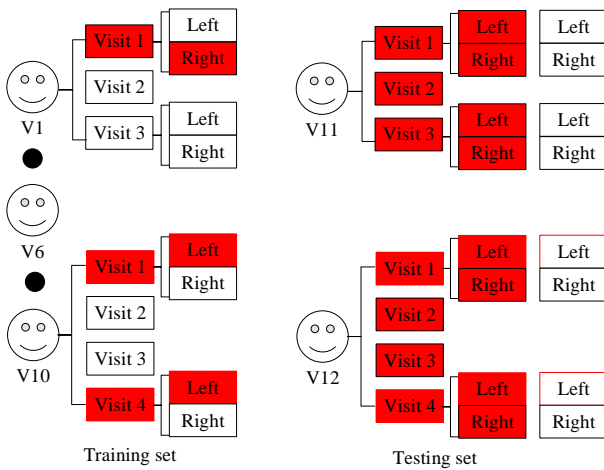


Fig. 4: One training-testing pair in which red blocks indicate randomly selected tumour visits and simulated tumour-bearing breasts, and white blocks indicate healthy visits and healthy breasts.

2.3 Parameter settings

As discussed in [19], signals collected by the antenna pairs located on the opposite sides of the breast can be highly dis-

torted and vary significantly among different volunteer visits. Thus, we discard signals from any antenna pair whose median peak amplitude of all the training data is less than a threshold of 20 mV. The signals are also truncated for the detection algorithm to focus on a region where tumour responses are most likely to occur. The windowing range is [61, 600] samples. These values are calculated as the feasible time period in which a tumour response can occur (see [19]). Excluding values outside this window reduces the noise during signal processing.

The candidate values of the 2ν -SVM hyper-parameters used for cross validation are listed in Table 2. We tested the detection performance with the γ value chosen from the candidate set $\gamma = \{2^{-15}, 2^{-13}, \dots, 2^5\}$ using a small subset of the data, and observed that the ensemble classifier almost always chose the γ values of $\{2^{-1}, 2^1\}$. We further tested a range of fixed γ values between 2^{-2} and 2^2 and observed that all gave similar performance. To reduce the computational cost during training, we set $\gamma = 1$ for the experiments detailed here.

Thus, there are $1 \times 18 \times 18 = 324$ different 2ν -SVM hyper-parameter combinations. These are used to produce a model library consisting of $M \times 324$ base models, where M is the number of retained antenna pairs in each data set. The ensemble classifier selects 100 base models, choosing those with the smallest Neyman-Pearson measure when applied to the training data, to perform classification on the test data.

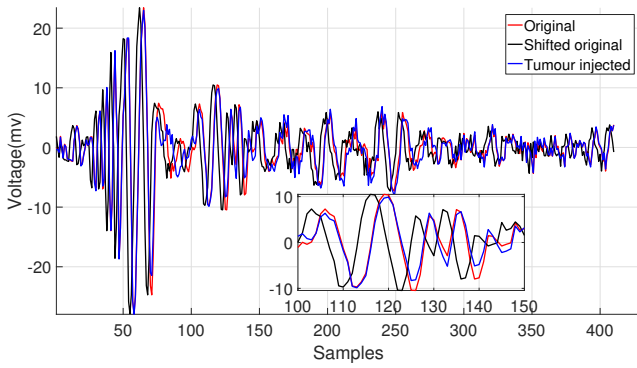
Table 2: Candidate values of hyper-parameters of 2ν -SVM in cross validation.

Parameter	Value
γ	1
ν_+	$1 \times 10^{-5}, 3 \times 10^{-5}, 1 \times 10^{-4}, 3 \times 10^{-4}, 0.001, 0.003, 0.01, 0.03, 0.1, 0.2, 0.3, \dots, 1$
ν_-	$1 \times 10^{-5}, 3 \times 10^{-5}, 1 \times 10^{-4}, 3 \times 10^{-4}, 0.001, 0.003, 0.01, 0.03, 0.1, 0.2, 0.3, \dots, 1$

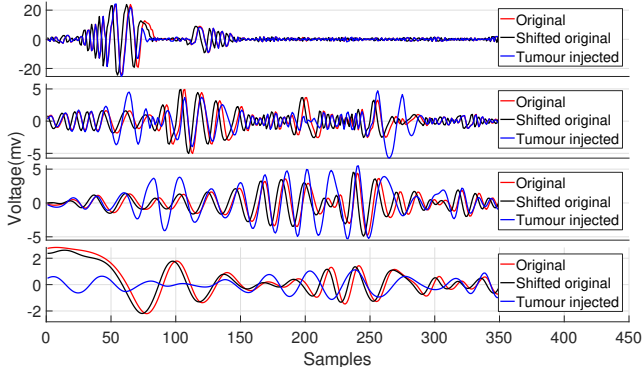
3 RESULTS

We first verify whether the EMD-based features are robust to signal misalignment. The EMD is applied to individual signals, so time shifts in one signal due to misalignment only affect the IMFs of that signal. In addition, the IMFs derived by the EMD are shift-invariant, in the sense that a shift in the input signal, provided it is an integer number of samples, will result in an equivalent shift in the IMFs. The features we have chose to derive from them are insensitive to these shifts. An example is shown in Figure 5 and Figure 6.

The EMD and PCA features extracted from the measurements in Figure 5a are shown in Figure 6. The figure shows



(a) An example of the original measurement, the original measurement shifted by four time samples, and the tumour response-injected measurement.



(b) The first four IMFs identified by EMD.

Fig. 5: Comparisons of IMFs derived from different measurements, including the original measurement, the shifted original measurement and the tumour response-injected measurement.

that the PCA features extracted from the original measurement and those from the tumour response-injected measurement are similar. The same observation applies for all other antenna pairs and tumour measurements. The classifier can perform much better if it is easier to discriminate between the features derived from the healthy and tumour response-injected measurements. Indeed, for PCA, there appears to be a greater discrepancy between the features of the original and time-shifted signals. For the EMD feature extraction, there is less discrepancy between the features derived from the original and time-shifted signals, and a greater distinction between the original and tumour response-injected measurements.

We evaluate the performance of the ensemble selection detection algorithm with EMD extracted features, PCA scores, and combined feature vectors from EMD and PCA, respectively. The detection performance with different α values is shown in Table 3. Irrespective of the features used, the ensemble selection detection algorithm almost always achieves an empirical false positive rate on the test data set that lies below the target false positive rate specified by α . The use

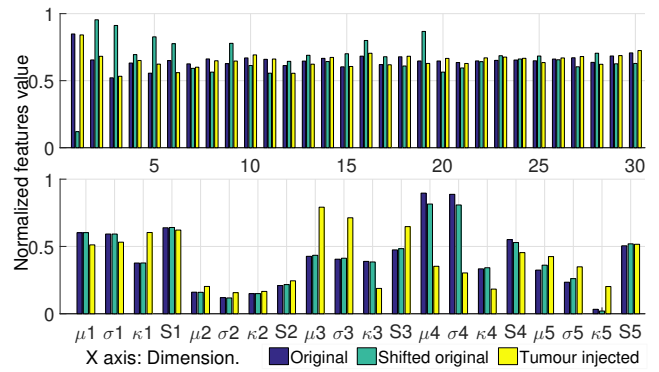


Fig. 6: Normalized EMD (bottom) and PCA features (top), X axis is dimension index.

of combined features (EMD and PCA) leads to the smallest miss probability and also the smallest Neyman-Pearson error for all three values of α .

Table 3: Average performance of three different kinds of features with different target false positive rates α . The 10% and 90% quantiles are shown in square brackets. The columns show the average false positive rate, the average false negative rate, the average error, and the average Neyman-Pearson error measure (Equation 5). Shaded entries indicate the smallest Neyman-Pearson error with the specific α .

α	Method	\hat{P}_F	\hat{P}_M	average error	\hat{e}
$\alpha=0.1$	EMD	0.03 [0.00, 0.10]	0.65 [0.44, 0.86]	0.34 [0.25, 0.44]	0.70 [0.45, 0.93]
	PCA	0.01 [0.00, 0.07]	0.63 [0.42, 0.83]	0.32 [0.21, 0.42]	0.65 [0.43, 0.86]
	EMD	0.02	0.59	0.31	0.62
	PCA	[0.00, 0.10]	[0.38, 0.81]	[0.21, 0.42]	[0.39, 0.85]
$\alpha=0.3$	EMD	0.09 [0.00, 0.22]	0.43 [0.21, 0.65]	0.27 [0.16, 0.37]	0.44 [0.22, 0.67]
	PCA	0.04 [0.00, 0.14]	0.57 [0.33, 0.79]	0.30 [0.18, 0.42]	0.57 [0.33, 0.78]
	EMD	0.09	0.40	0.24	0.40
	PCA	[0.00, 0.21]	[0.18, 0.60]	[0.14, 0.35]	[0.19, 0.62]
$\alpha=0.5$	EMD	0.21 [0.00, 0.4]	0.27 [0.08, 0.50]	0.24 [0.14, 0.35]	0.28 [0.08, 0.5]
	PCA	0.14 [0.00, 0.36]	0.52 [0.29, 0.75]	0.33 [0.19, 0.46]	0.53 [0.30, 0.75]
	EMD	0.18	0.26	0.22	0.27
	PCA	[0.00, 0.36]	[0.07, 0.45]	[0.10, 0.32]	[0.07, 0.45]

If we vary α over 101 evenly-spaced values between 0 and 1, we obtain different false positive rates and true positive rates on the test data. These form different operating points in the receiver operating characteristic (ROC) curves. Figure 7 shows the ROC curves, averaged over the 50 data sets, for the three choices of features. The areas-under-curve (AUCs) with EMD extracted features, PCA scores and combined features are 0.83, 0.70, and 0.87, respectively.

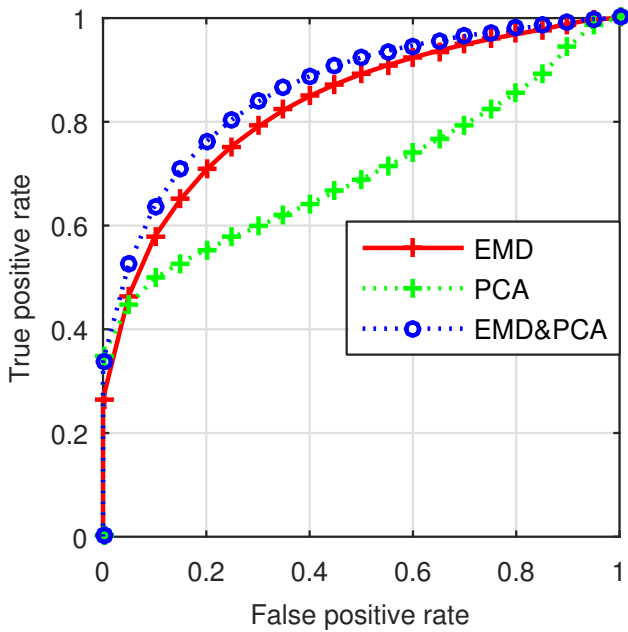


Fig. 7: Average receiver operating characteristic (ROC) curves for different features (EMD, PCA, and combined EMD and PCA) for the tumour response-injected clinical data with $\Gamma = 1$.

We are also interested in examining whether the detection performance is consistent across volunteers. It is important to check that the algorithms do not consistently fail to detect tumours for one of the volunteers. Figure 8 shows the detection error, averaged over the 50 constructed datasets, for three choices of α .

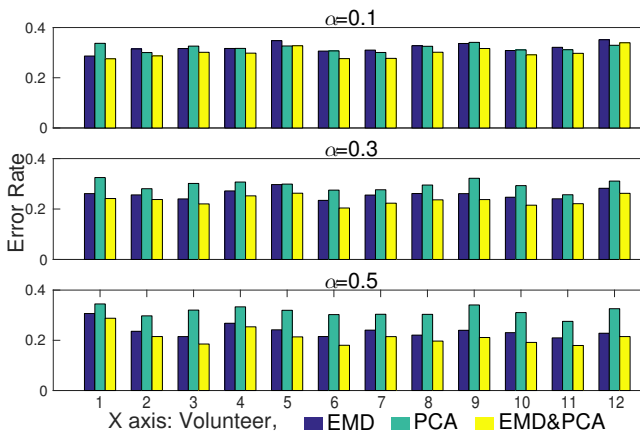


Fig. 8: The test-set (generalized) detection error for each volunteer, averaged over 50 data sets, for three choices of α .

To investigate which EMD features are most useful, we separate the 1×20 EMD-extracted feature vector for each

antenna pair into 20 scalar features. Thus, the ensemble selection algorithm will be able to select those EMD features that are most useful in reducing the training errors. The experiment is carried out on eight randomly selected data sets. Figure 9 displays the frequency of different features selected by the ensemble selection classifier. We observe that the mean absolute value and standard deviation from 5 IMFs are most likely to be selected. We compare the results from combined features from PCA and EMD with the results from scalar features. The ROC curves, averaged over the 20 data sets, are shown in Figure 10.

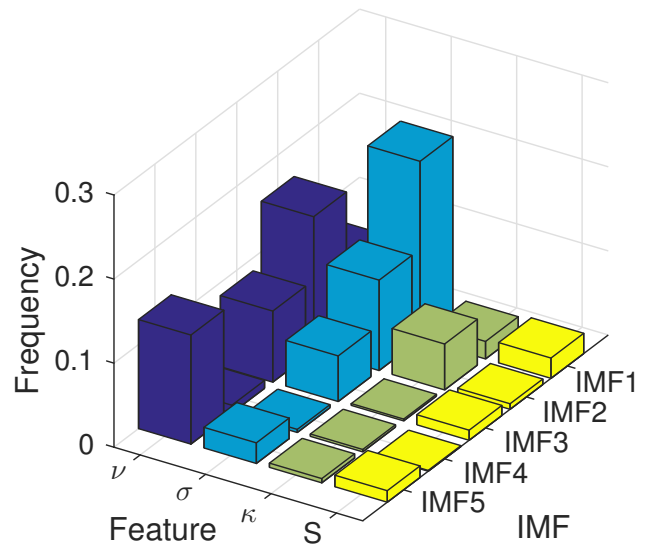


Fig. 9: Distribution of the features that are selected by the ensemble classifier for the case when the EMD features are separated into individual scalar features.

The final investigation we conducted is to assess the performance of the combined features (EMD and PCA) on data sets with lower signal-to-noise ratio (SNR). The lower SNR signals can be constructed by reducing the value of Γ in Equation (6). We generated 20 data sets with $\Gamma = 0.75$ and 20 data sets with $\Gamma = 0.5$, respectively. The ROC curves, averaged over the 20 data sets, are shown in Figure 11.

4 Discussion

We observe from results reported in Section 3 that the use of EMD-extracted features results in significantly better detection performance compared to features based on PCA. A slight improvement over EMD features can be achieved by using the combined EMD and PCA features. As illustrated in Figure 10, better detection performance is observed when all EMD-extracted features from one antenna pair are combined into a single feature vector.

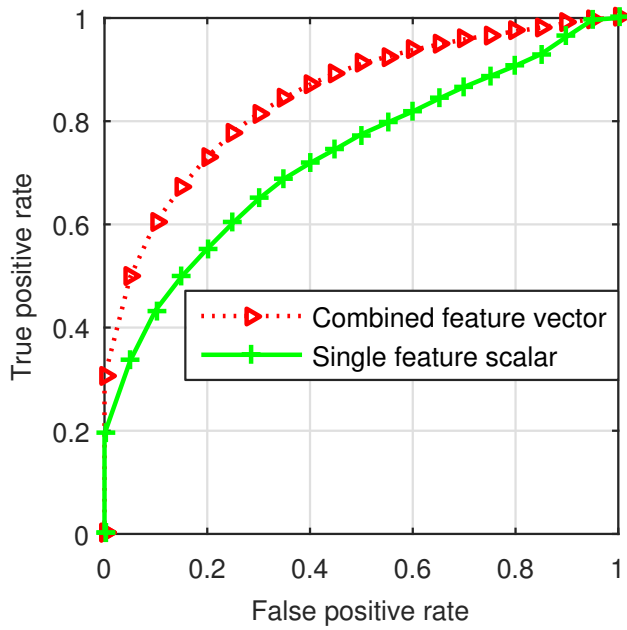


Fig. 10: The ROC curves, averaged over 20 datasets with $\Gamma = 1$, for the cases of (i) a combined EMD and PCA feature vector (50 elements) and (ii) 20 individual EMD scalar features.

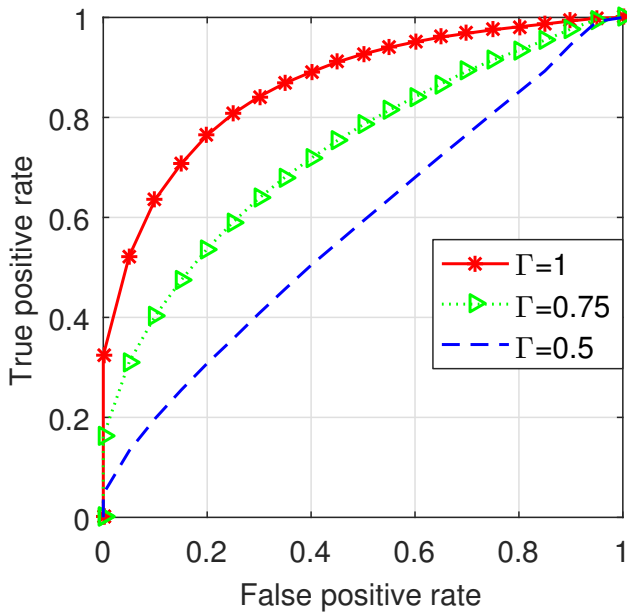


Fig. 11: The ROC curves, averaged over 20 data sets, for the case of combined EMD and PCA features, for three different values of Γ .

The average detection error is similar for all volunteers, irrespective of the features employed, as shown in Figure 8. We have also observed (results not shown) that the detection algorithms have consistent performance with respect to tumour locations, which are randomly generated in the upper outer quadrant of the breast hemispherical model.

It is observed in Figure 11 that the reduced signal-to-noise ratio leads to significantly poorer detection performance, but the performance degradation is graceful. When $\Gamma = 0.5$, the detection performance is only slightly better than a random guess. Although experiments with phantoms suggest that a choice of $\Gamma = 1$ is reasonable, the appropriate value is dictated by the contrast between tumorous and healthy tissue, and there is still considerable uncertainty about the extent of this contrast. The performance deterioration motivates the development of feature extraction methods and detection algorithms that can better tackle these lower signal-to-noise scenarios.

5 Conclusion

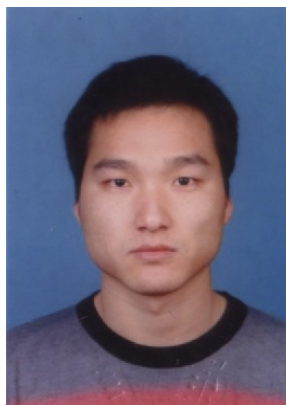
In this paper, we proposed and explored the use of an EMD-based feature extraction method for microwave breast tumour detection. We were motivated to explore the use of EMD features because of their potential robustness to the system jitter common in microwave breast cancer scans. We evaluated detection performance using EMD-based features and the commonly-used PCA features using a clinical trial data collected over an eight-month span combined with a numerical tumour response construction method. We observe that the use of features based on the EMD leads to significantly improved detection performance compared to PCA-based features. A marginal additional improvement can be achieved by using a combination of EMD and PCA features.

Acknowledgements Hongchao Song is sponsored by the China Scholarship Council and the Postgraduate Innovation Fund of SICE, BUPT, 2015.

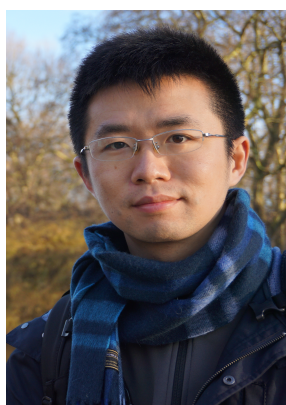
References

1. AlShehri, S.A., Khatun, S., Jantan, A.B., Raja Abdullah, R.S.A., Mahmud, R., Awang, Z.: Experimental breast tumor detection using NN-based UWB imaging. *Prog Electromagn Res (PIER)* **111**, 447–465 (2011)
2. Bajaj, V., Pachori, R.B.: Classification of seizure and nonseizure EEG signals using empirical mode decomposition. *IEEE T Inf Technol B* **16**(6), 1135–1142 (2012)
3. Bourqui, J., Sill, J.M., Fear, E.C.: A prototype system for measuring microwave frequency reflections from the breast. *International Journal of Biomedical Imaging* **2012**, 9 (2012)
4. Byrne, D., Craddock, I.J.: Time-domain wideband adaptive beamforming for radar breast imaging. *IEEE T Antenn Propag* **63**(4), 1725–1735 (2015)

5. Byrne, D., O'Halloran, M., Glavin, M., Jones, E.: Breast cancer detection based on differential ultrawideband microwave radar. *Prog Electromagn Res M (PIER-M)* **20**, 231–242 (2011)
6. Caorsi, S., Gagnani, G.L., Pastorino, M.: Reconstruction of dielectric permittivity distributions in arbitrary 2-D inhomogeneous biological bodies by a multiview microwave numerical method. *IEEE T Med Imaging* **12**(2), 232–239 (1993)
7. Chew, H.G., Bogner, R.E., Lim, C.C.: Dual ν -support vector machine with error rate and training size biasing. In: *Int Conf Acoust Spee (ICASSP)*, pp. 1269–1272. Salt Lake City, UT (2001)
8. Conceicao, R.C., Medeiros, H., O'Halloran, M., Rodriguez-Herrera, D., Flores-Tapia, D., Pistorius, S.: Initial classification of breast tumour phantoms using a UWB radar prototype. In: *Proc. Int. Conf. Electromagnetics in Advanced Applications (ICEAA)*, pp. 720–723. Singapore (2013)
9. Conceição, R.C., Medeiros, H., O'Halloran, M., Rodriguez-Herrera, D., Flores-Tapia, D., Pistorius, S.: SVM-based classification of breast tumour phantoms using a UWB radar prototype system. In: *Proc. URSI General Assembly and Scientific Symposium (GASS)*, pp. 1–4. Beijing, China (2014)
10. Davis, S.K., Tandradinata, H., Hagness, S.C., Van Veen, B.D.: Ultrawideband microwave breast cancer detection: a detection-theoretic approach using the generalized likelihood ratio test. *IEEE T Bio-Med Eng* **52**(7), 1237–1250 (2005)
11. Davis, S.K., Van Veen, B.D., Hagness, S.C., Kelcz, F.: Breast tumor characterization based on ultrawideband microwave backscatter. *IEEE T Bio-Med Eng* **55**(1), 237–246 (2008)
12. Debye, P.J.W.: *Polar molecules*. The Chemical Catalog CO., New York (1929)
13. Hagness, S., Leininger, K., Booske, J., Okoniewski, M.: Dielectric characterization of human breast tissue at microwave frequencies. In: *Proc. 2nd Int. World Congr. Microwave and Radio Frequency Process*. Orlando, FL (2000)
14. Huang, N.E., Shen, Z., Long, S.R., Wu, M.C., Shih, H.H., Zheng, Q., Yen, N.C., Tung, C.C., Liu, H.H.: The empirical mode decomposition and the hilbert spectrum for nonlinear and non-stationary time series analysis. *Proc. Roy. Soc. London A: Math., Physical and Eng. Sci.* **454**, 903–995 (1998)
15. Klemm, M., Craddock, I., Leendertz, J., Preece, A., Gibbins, D., Shere, M., Benjamin, R.: Clinical trials of a UWB imaging radar for breast cancer. In: *European Conference on Antennas and Propagation (EuCAP)*, pp. 1–4. Barcelona, Spain (2010)
16. Kosmas, P., Rappaport, C.M.: FDTD-based time reversal for microwave breast cancer detection-localization in three dimensions. *IEEE T Microw Theory* **54**(4), 1921–1927 (2006)
17. Li, S., Zhou, W., Yuan, Q., Geng, S., Cai, D.: Feature extraction and recognition of ictal EEG using EMD and SVM. *Comput Biol Med* **43**(7), 807–816 (2013)
18. Li, X., Hagness, S.C.: A confocal microwave imaging algorithm for breast cancer detection. *IEEE Microw Wirel Co* **11**(3), 130–132 (2001)
19. Li, Y., Porter, E., Santorelli, A., Popović, M., Coates, M.: Microwave breast cancer detection via cost-sensitive ensemble classifiers: Phantom and patient investigation. *BIOMED SIGNAL PROCES* **31**, 366–376 (2017)
20. Li, Y., Santorelli, A., Laforest, O., Coates, M.: Cost-sensitive ensemble classifiers for microwave breast cancer detection. In: *Int Conf Acoust Spee (ICASSP)*. Brisbane, Australia (2015)
21. Lim, H.B., Nhung, N.T.T., Li, E.P., Thang, N.D.: Confocal microwave imaging for breast cancer detection: Delay-multiply-and-sum image reconstruction algorithm. *IEEE T Bio-Med Eng* **55**(6), 1697–1704 (2008)
22. Meaney, P.M., Fanning, M.W., Raynolds, T., Fox, C.J., Fang, Q., Kogel, C.A., Poplack, S.P., Paulsen, K.D.: Initial clinical experience with microwave breast imaging in women with normal mamography. *Acad Radiol* **14**(2), 207–218 (2007)
23. O'Halloran, M., Jones, E., Glavin, M.: Quasi-multistatic MIST beamforming for the early detection of breast cancer. *IEEE T Bio-Med Eng* **57**(4), 830–840 (2010)
24. Porter, E., Coates, M., Popović, M.: An early clinical study of time-domain microwave radar for breast health monitoring. *IEEE T Bio-Med Eng* **63**(3), 530–539 (2016)
25. Porter, E., Kirshin, E., Santorelli, A., Coates, M., Popovic, M.: Time-domain multistatic radar system for microwave breast screening. *IEEE Antenn Wirel Pr* **12**, 229–232 (2013)
26. Porter, E., Kirshin, E., Santorelli, A., Popović, M.: Microwave breast screening in the time domain: identification and compensation of measurement-induced uncertainties. *Prog Electromagn Res B (PIER-B)* **55**, 115–130 (2016)
27. Canadian Cancer Society's Advisory Committee on Cancer Statistics: *Canadian cancer statistics 2015*. Canadian Cancer Society, Toronto, ON (2015)
28. Santorelli, A., Kirshin, E., Porter, E., Popović, M., Schwartz, J.: Improved calibration for an experimental time-domain microwave imaging system. In: *European Conference on Antennas and Propagation (EuCAP)*. Gothenburg, Sweden (2013)
29. Scott, C.: Performance measures for Neyman-Pearson classification. *IEEE T Inform Theory* **53**, 2852–2863 (2007)
30. Shea, J.D., Kosmas, P., Hagness, S.C., Van Veen, B.D.: Three-dimensional microwave imaging of realistic numerical breast phantoms via a multiple-frequency inverse scattering technique. *Med Phys* **37**(8), 4210–4226 (2010)
31. Sohn, V.Y., Arthurs, Z.M., Sebesta, J.A., Brown, T.A.: Primary tumor location impacts breast cancer survival. *The American Journal of Surgery* **195**(5), 641–644 (2008)
32. Sugitani, T., Kubota, S.i., Kuroki, S.i., Sogo, K., Arihiro, K., Okada, M., Kadoya, T., Hide, M., Oda, M., Kikkawa, T.: Complex permittivities of breast tumor tissues obtained from cancer surgeries. *Appl Phys Lett* **104**(25), 253,702 (2014)



Hongchao Song is currently a PhD candidate in Beijing University of Posts and Telecommunications. From 2015 to 2016, He was a visiting Ph.D. student with the McGill University. His research interests include microwave-based breast cancer detection and digital image processing.



Yunpeng Li joined McGill University to pursue a Ph.D. degree in electrical engineering, from September 2012. His current research is on microwave-based breast cancer detection and particle filtering.



Mark Coates is an Associate Professor at McGill University, Canada. He received a B.E. from the University of Adelaide, Australia (1995), and a Ph.D. from the University of Cambridge, U.K., in 1999.



Aidong Men is a Professor at Beijing University of Posts and Telecommunications, China, where he received his Ph.D in 1994.